

Magnetorotational Collapse of Population III Stars

Yudai SUWA¹, Tomoya TAKIWAKI¹, Kei KOTAKE², and, Katsuhiko SATO^{1,3}

¹*Department of Physics, School of Science, The University of Tokyo, Tokyo 113-0033*

²*National Astronomical Observatory of Japan, Mitaka, Tokyo 181-8588, Japan*

³*Research Center for the Early Universe, School of Science, the University of Tokyo, 7-3-1 Hongo, Bunkyo-ku, Tokyo 113-0033, Japan*
suwa@utap.phys.s.u-tokyo.ac.jp

(Received 2006 October 12; accepted 2007 April 11)

Abstract

We perform a series of two-dimensional magnetorotational core-collapse simulations of Pop III stars. Changing the initial distributions of rotation and magnetic fields prior to collapse in a parametric manner, we compute 19 models. By so doing, we systematically investigate how rotation and magnetic fields affect the collapse dynamics and explore how the properties of the black-hole formations and neutrino emissions could be affected. As for the microphysics, we employ a realistic equation of state and approximate the neutrino transfer by a multiflavour leakage scheme. With these computations, we find that the jet-like explosions are obtained by the magneto-driven shock waves if the initial magnetic field is as large as 10^{12}G . We point out that the black-hole masses at the formation decrease with the initial field strength, on the other hand, increase with the initial rotation rates. As for the neutrino properties, we point out that the degree of the differential rotation plays an important role to determine which species of the neutrino luminosity is more dominant than the others. Furthermore, we find that the stronger magnetic fields make the peak neutrino luminosities smaller, because the magnetic pressure acts to halt the collapse in the central regions, leading to the suppression of the releasable gravitational binding energies.

Key words: stars: supernovae: general — black hole physics — neutrinos — methods: numerical — magnetohydrodynamics: MHD

1. INTRODUCTION

Great attention has been paid to Population III, the first stars to form in the universe, because they are related to many unsettled problems in cosmology and the stellar physics. The Population III (Pop III) stars ionize and enrich the metallicity of the intergalactic medium and thus provide important clues to the subsequent star formation history (for reviews, see e.g.,

Barkana & Loeb 2001; Bromm & Larson 2004; Glover 2005). Pop III stars are also important for the understanding of the chemical evolution history. Recent discovery of hyper metal poor stars such as HE 0107-5240 (Christlieb et al. 2002) and HE 1327-2326 (Frebel et al. 2005) has given us good opportunities to investigate the nucleosynthesis in Pop III stars (Heger & Woosley 2002; Umeda & Nomoto 2002; Umeda & Nomoto 2003; Daigne et al. 2004; Iwamoto et al. 2005). Gamma-ray bursts at very high redshift are pointed out to be accompanied by the gravitational collapse of Pop III stars (Schneider et al. 2002; Bromm & Loeb 2006). The *Swift* satellite, which is now running ¹, is expected to directly detect the Pop III stars accompanied by the high-*z* gamma-ray bursts.

The evolutions of Pop III stars have been also studied for long. From their studies, Pop III stars are predicted to have been predominantly very massive with $M \gtrsim 100M_{\odot}$ (Nakamura & Umemura 2001; Abel et al. 2002; Bromm et al. 2002, see references therein). Massive stars in the range of $100M_{\odot} \lesssim M \lesssim 260M_{\odot}$ encounter the electron-positron pair instability during their evolution. This instability sets off explosive oxygen burning, and if the burning provides enough energy to reverse the collapse, the stars are thought to become pair instability supernovae (Bond et al. 1984; Fryer et al. 2001; Heger & Woosley 2002), whose detectability has been recently reported (Scannapieco et al. 2005; Weinmann & Lilly 2005). More massive stars, which also encounter pair-instability, are so tightly bound and the fusion of oxygen is unable to reverse infall. Such stars are thought to collapse to black holes (BHs) finally (Bond et al. 1984; Fryer et al. 2001), which we pay attention to in this paper.

So far there have been a few hydrodynamic simulations studying the gravitational-collapse of the BH forming Pop III stars. In the two-dimensional, gray neutrino transport simulations by Fryer et al. (2001), they investigated the collapse of a rotating Pop III star of $300M_{\odot}$, leading to the BH formation. They discussed the effects of rotation on the emitted neutrino luminosities, gravitational waves, and furthermore, the possibility of such stars to be the gamma-ray bursts. In their Newtonian study, the central BH was excised and treated as an absorbing boundary after the formation. Although such simplification is not easy to be validated, they followed the dynamics long after the formation of the BH and obtained many findings. More recently, Nakazato et al. (2006) performed one-dimensional, but, general relativistic simulations in the range of $100 \sim 10000M_{\odot}$, in which the state-of-the-art neutrino physics are taken into account. Their detailed calculations revealed the properties of the emergent neutrino spectrum, and based on that, they discussed the detectability of such neutrinos as the supernova relic neutrino background (see also Ando & Sato 2004; Iocco et al. 2005). They successfully saw the formation of the apparent horizon, however, the dynamics in the later phases was not referred.

In this paper we study the magnetorotational collapse of Pop III stars by performing the two-dimensional magnetohydrodynamic (MHD) simulations (see, also, Akiyama et al. 2003;

¹ See <http://swift.gsfc.nasa.gov>

Kotake et al. 2004a; Kotake et al. 2004b; Takiwaki et al. 2004; Yamada & Sawai 2004; Ardeljan et al. 2005; Sawai et al. 2005; Obergaulinger et al. 2006, for MHD computations of core-collapse supernovae, and Kotake et al. 2006 for a review). As for the microphysics, we employ a realistic equation of state based on the relativistic mean field theory and take into account the neutrino cooling by a multiflavor leakage scheme, in which state-of-the-art reactions of neutrinos are included. In our Newtonian simulations, the formation of the BHs is ascribed to a certain condition, and after the formation, the central region is excised and treated as an absorbing boundary in order to follow the dynamics later on. Since the distributions of rotation and magnetic fields in the progenitors of Pop III stars are highly uncertain, we change them in a parametric manner and systematically investigate how rotation and magnetic fields affect the dynamics. We also explore how the natures of explosions, the properties of the BHs and neutrino luminosities could be affected due to the incursion of the rotation and magnetic fields.

This paper is organized as follows. In §2, we describe the numerical methods and the initial conditions. In §3, we present the results. We give a summary and discussion in §4.

2. METHOD

2.1. Basic Equations

The basic evolution equations are written as follows,

$$\frac{d\rho}{dt} + \rho \nabla \cdot \mathbf{v} = 0, \quad (1)$$

$$\rho \frac{d\mathbf{v}}{dt} = -\nabla P - \rho \nabla \Phi + \frac{1}{4\pi} (\nabla \times \mathbf{B}) \times \mathbf{B}, \quad (2)$$

$$\rho \frac{d}{dt} \left(\frac{e}{\rho} \right) = -P \nabla \cdot \mathbf{v} - L_\nu, \quad (3)$$

$$\frac{\partial \mathbf{B}}{\partial t} = \nabla \times (\mathbf{v} \times \mathbf{B}), \quad (4)$$

$$\Delta \Phi = 4\pi G \rho, \quad (5)$$

where $\rho, P, \mathbf{v}, e, \Phi, \mathbf{B}, L_\nu, \frac{d}{dt}$, are the mass density, the gas pressure including the radiation pressure from neutrino's, the fluid velocity, the internal energy density, the gravitational potential, the magnetic field, the neutrino cooling rate, and Lagrange derivative, respectively. In our 2D calculations, axial symmetry and reflection symmetry across the equatorial plane are assumed. Spherical coordinates (r, θ) are employed with logarithmic zoning in the radial direction and regular zoning in θ . One quadrant of the meridian section is covered with $300 (r) \times 30 (\theta)$ mesh points. The minimum and maximum mesh spacings are 2 km and 60 km, respectively. We also calculated some models with 60 angular mesh points, however, any significant difference was obtained. Therefore, we will report in the following the results obtained from the models with 30 angular mesh points. We employed the ZEUS-2D code (Stone & Norman 1992) as a base

and added major changes to include the microphysics. First we added an equation for electron fraction to treat electron captures and neutrino transport by the so-called leakage scheme (Kotake et al. 2003). Furthermore, we extend the scheme to include all 6 species of neutrino ($\nu_e, \bar{\nu}_e, \nu_X$), which is indispensable for the computations of the Pop III stars. Here ν_X means $\nu_\mu, \bar{\nu}_\mu, \nu_\tau$ and $\bar{\nu}_\tau$. As for the reactions of ν_X , pair, photo, and plasma processes are included using the rates by Itoh et al. (1989). The L_ν , in Eq. (3) is the cooling rate of the relevant neutrino reactions (see Takiwaki et al. 2007, for details). As for the equation of state, we have incorporated the tabulated one based on relativistic mean field theory instead of the ideal gas EOS assumed in the original code (Shen et al. 1998).

2.2. Initial Models and Boundary Condition

In this paper, we set the mass of the Pop III star to be $300M_\odot$. This is consistent with the recent simulations of the star-formation phenomena in a metal free environment, providing an initial mass function peaked at masses $100 - 300M_\odot$ (see, e.g., Nakamura & Umemura 2001). We choose the value because we do not treat the nuclear-powered pair instability supernovae ($M \lesssim 260M_\odot$) and, for convenience, for the comparison with the previous study, which employed the same stellar mass (Fryer et al. 2001).

We start the collapse simulations of $180M_\odot$ core of the $300M_\odot$ star. The core, which is the initial condition of our simulations, is produced in the following way. According to the prescription in Bond et al. (1984), we set the polytropic index of the core to $n = 3$ and assume that the core is isentropic of $\sim 10k_B$ per nucleon (Fryer et al. 2001) with the constant electron fraction of $Y_e = 0.5$. We adjust central density to $5 \times 10^6 \text{ g cm}^{-3}$, by which the temperature of the central regions become high enough to photodisintegrate the iron ($\sim 5 \times 10^9 \text{ K}$), thus initiating the collapse. Given central density, the distribution of electron fraction, and entropy, we construct numerically the hydrostatic structures of the core.

Since we know little of the angular momentum distributions in the cores of Pop III stars (see, however, Fryer et al. 2001), we add the following rotation profiles in a parametric manner to the non-rotating core mentioned above. We assume the cylindrical rotation of the core and change the degree of differential rotation in the following two ways.

1. As for the differential rotation models, we assume the following distribution of the initial angular velocity,

$$\Omega(X, Z) = \Omega_0 \frac{X_0^2}{X^2 + X_0^2} \frac{Z_0^4}{Z^4 + Z_0^4}, \quad (6)$$

where Ω is the angular velocity and Ω_0 is the model constant. X and Z denote distance from rotational axis and the equatorial plane, respectively. We adopt the value of parameters, X_0 and Z_0 , as $2 \times 10^8 \text{ cm}$, $2 \times 10^9 \text{ cm}$, respectively. Since the radius of the outer edge of the core is taken to be as large as $3.5 \times 10^9 \text{ cm}$, the above profile represents that the cores rotate strongly differentially.

2. As for the rigid rotation models, the initial angular velocity is given by,

$$\Omega(X, Z) = \Omega_0. \quad (7)$$

As for the initial configuration of the magnetic fields, we assume that the field is nearly uniform and parallel to the rotational axis in the core and dipolar outside (see Figure 1). For the purpose, we consider the following effective vector potential,

$$A_r = A_\theta = 0, \quad (8)$$

$$A_\phi = \frac{B_0}{2} \frac{r_0^3}{r^3 + r_0^3} r \sin \theta, \quad (9)$$

where $A_{r,\theta,\phi}$ is the vector potential in the r, θ, ϕ direction, respectively, r is the radius, r_0 is the radius of the core, and B_0 is the model constant. In this study, we adopt the value of r_0 as 3.5×10^9 cm. This vector potential can produce the uniform magnetic fields when r is small compared with r_0 , and the dipole magnetic fields for vice versa. We set the outflow boundary conditions for the magnetic fields at the outer boundary of the calculated regions. It is noted that this is a far better way than the loop current method for constructing the dipole magnetic fields (LeBlanc & Wilson 1970), because our method produces no divergence of the magnetic fields near the loop current.

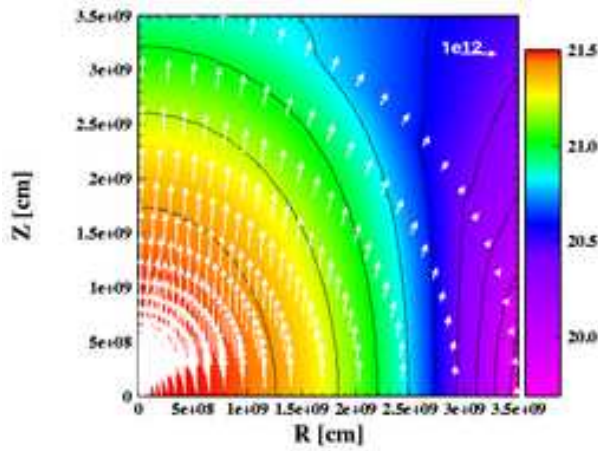


Fig. 1. The configuration of the initial magnetic fields. Note that $B_0 = 10^{12}$ G for this figure. The arrows represent the vector of the poloidal magnetic fields. The contour shows the logarithm of the magnetic pressure ($: B^2/8\pi$).

Changing the initial rotational and magnetic energies by varying the values of Ω_0 and B_0 , we compute 19 models in this paper, namely, one spherical and 18 magnetorotational models. In Table 1, we summarize the differences of the initial models. Note that the models are named after this combination, with the first letters, B12, B11, B10, indicating the strength of initial magnetic field, the following letter, TW1, TW2, TW4 indicating the initial $T/|W|$ and final capital letter D or R representing the initial rotational law (D: Differential rotation, R: Rigid

rotation). Note that $T/|W|$ represents the ratio of the rotational to the gravitational energy.

Table 1. Models and Parameters.*

B_0	$T/ W $		
	1%	2%	4%
10^{10}G	B10TW1{D,R}	B10TW2{D,R}	B10TW4{D,R}
10^{11}G	B11TW1{D,R}	B11TW2{D,R}	B11TW4{D,R}
10^{12}G	B12TW1{D,R}	B12TW2{D,R}	B12TW4{D,R}

* This table shows the name of the models. In the table they are labeled by the strength of the initial magnetic field and rotation. $T/|W|$ represents the ratio of the rotational to the gravitational energy. B_0 represents the strength of the initial magnetic field.

In this paper we assume a BH is formed when the condition $\frac{6Gm(r)}{c^2} > r$ is satisfied, where $c, G, m(r)$ are the speed of light, the gravitational constant and the mass coordinate, respectively. This condition means that we assume that fluids cannot escape from the inner region below the radius of the marginally stable orbit of a Schwarzschild BH. When this condition is satisfied, we excise the region inside the radius calculated and then treat it as an absorbing boundary. Afterwards, we enlarge the boundary of the excised region to take into account the growth of the mass infalling into the central region. Although it is not accurate at all to refer the central region as the BH, we cling to the simplification in this paper in order to follow and see the dynamics later on.

3. RESULT

3.1. Spherical Collapse

First of all, we briefly describe the hydrodynamic features of spherical collapse as a baseline for the MHD models mentioned later. Note in the following that by “massive stars”, we mean the stars of $\approx O(10)M_\odot$ with the initial composition of the solar metallicity, which are considered to explode as supernovae at their ends of the evolution (Heger et al. 2003).

As in the case of massive stars, the gravitational collapse is triggered by the electron-capture reactions and the photodisintegration of iron nuclei. On the other hand, the gravitational contraction is stopped not by the nuclear forces as in the case of massive stars but by the (gradient of) thermal pressure. This is because the progenitor of Pop III stars has high entropy, i.e. high temperature. We call this bounce as “thermal bounce” for convenience. The evolution of density, temperature, entropy and radial velocity around the thermal bounce are shown in Figure 2. Unlike the case of massive stars, no outgoing shock propagates outward after the thermal bounce. At the bounce, the size of the inner core, which is 200 km in radius and $6M_\odot$ in the masscoordinate, grows gradually due to the mass accretion. As seen from the figure, the materials in the accreting shock regions obtain higher entropy and temperature than

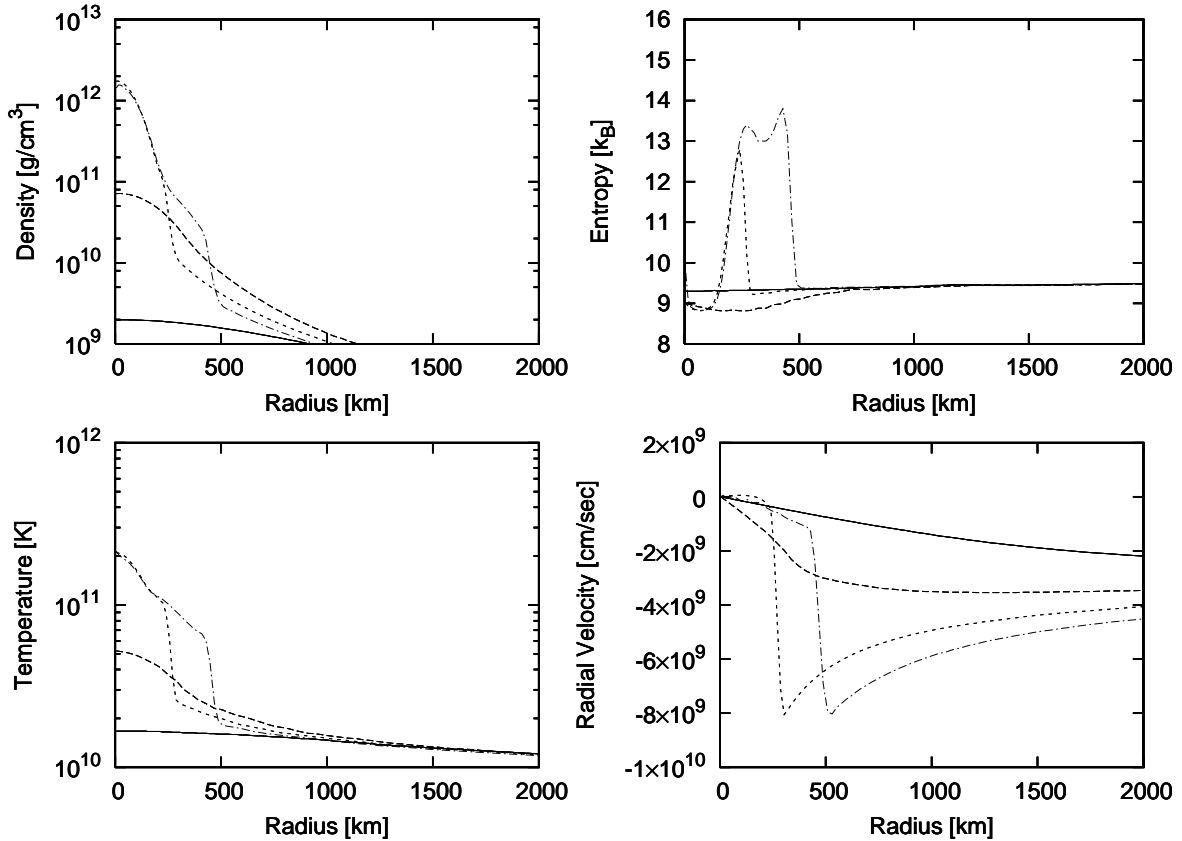


Fig. 2. The evolutions of density, temperature, entropy and radial velocities in the spherical model. Solid line is for -37 ms from bounce, dashed line is for -1 ms, dotted line is for 19 ms and dashed dotted line is for 32 ms, respectively.

the ones in the case of massive stars.

The higher temperatures are good for producing a large amount of μ - and τ - neutrinos through the pair annihilation of electrons and positrons. This also makes different features of the neutrino emissions from the case of massive stars, in which the electron-neutrino (ν_e) luminosity dominates over those of the other species near the epoch of core bounce. As shown in the top panel of Figure 3, the total luminosity of ν_X (ν_μ , ν_τ , $\bar{\nu}_\mu$ and $\bar{\nu}_\tau$) begins to dominate over the total luminosity of electron neutrinos and anti-electron neutrinos at 25 msec after bounce (see the first intersection of the lines in the figure).

At 87 msec after the bounce, the core is so heavy that it promptly collapses to a BH. In Figure 4, we show the evolution of the BH calculated by the procedure described in §2.2. The mass of the BH is initially $20M_\odot$, rapidly increases to $35M_\odot$ because the rest of the dense inner core falls into the BH soon after the formation. The growth rate of the mass is slowed down afterwards when the quasi-steady accretion flow to the BH is established (Fig 4). The rapid decrease of the neutrino luminosity ~ 100 msec after bounce (top panel of Figure 3) corresponds to the epoch when the neutrinospheres are swallowed into the BH. Note in the bottom panel,

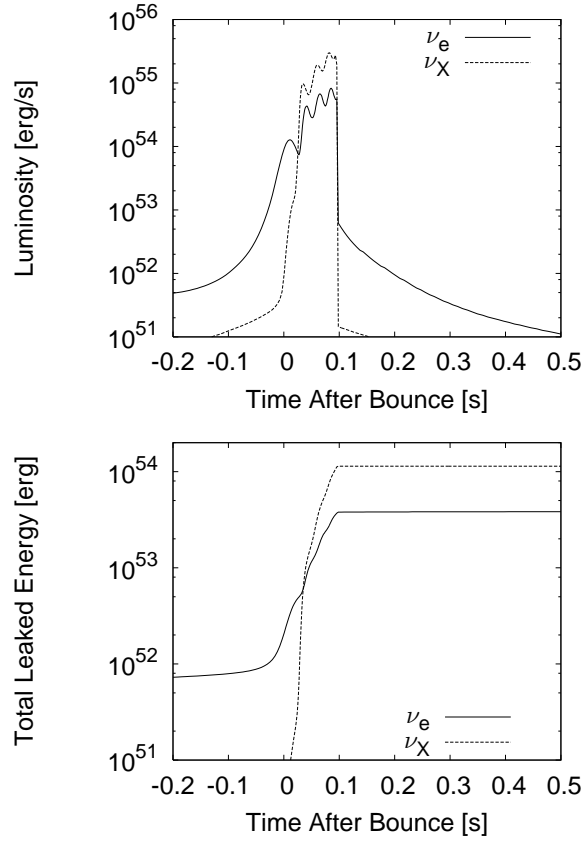


Fig. 3. *Upper panel:* Time evolutions of neutrino luminosity in the spherical model. The time is measured from the thermal bounce. Solid line represents the total luminosity of electron neutrinos and anti-electron neutrinos. Dashed line represents the total luminosity of ν_X (ν_μ , ν_τ , $\bar{\nu}_\mu$ and $\bar{\nu}_\tau$) neutrino. Before the thermal bounce, the luminosity of electron + anti-electron neutrinos dominate that of ν_X luminosity, though, after the bounce, it reverses. At ~ 0.1 second after the bounce, the luminosities drastically decrease due to the BH formation. *Lower panel:* Time-integrated neutrino luminosities. Solid line and Dashed line are total energy emitted by electron neutrinos and anti-electron neutrinos and X neutrinos, respectively.

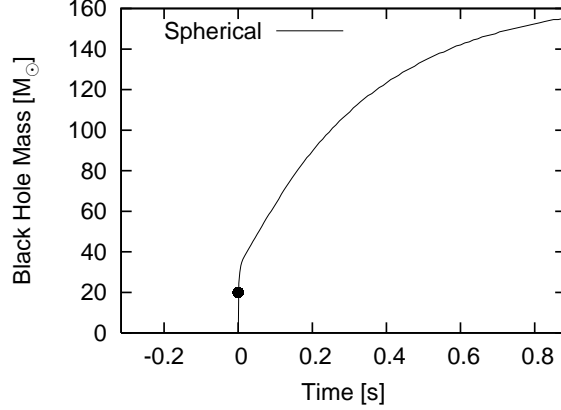


Fig. 4. Evolution of the BH mass in the spherical model. The time is measured from the BH formation. The black filled circle indicates the epoch of the black-hole formation.

the total emitted energy are calculated by $\int dt L_\nu$, which represents the energy carried out from the core by neutrinos. Again from the quantity, it is shown that ν_X deprives dominantly of the gravitational energy of the core than ν_e and $\bar{\nu}_e$.

3.2. Rotational Collapse

3.2.1. Effect of Differential Rotation

Now we move on to discuss the features in the rotational core-collapse. The deviation of the dynamics from the spherical collapse comes from the initial rotation rates and the degree of the differential rotation initially imposed. To see the effects of the differential rotation on the collapse-dynamics, we first take models of B10TW1D (differential rotation) and B10TW1R (rigid rotation) as examples and mention the difference of them. The effects of the initial rotation rates are discussed later in §3.2.2.

We first describe the collapse of model B10TW1D. As in the case of spherical collapse, the rotating core experiences the collapse due to the neutrino emission and the photodisintegration, but the difference appears at the time of the thermal bounce. Due to the pressure support supplied by the centrifugal force, model B10TW1D bounces at the pole at the epoch 17 msec later than that of the spherical collapse. The time evolutions after bounce is presented in Figure 5. It is shown that the materials of the inner core oscillate about 20 msec after bounce (see from the top left down to the bottom), and then the shock wave begins to propagate along the rotational axis (see from the top right down to the bottom). This jet-like shock wave finally stalls at $Z \sim 2 \times 10^8$ cm, where Z is the distance from the center along the rotational axis. It is noted that the shock wave formed at bounce does not stall in the strongly magnetized models as discussed in §3.3. In this weakly magnetized model, the stellar mantle just collapses to the central region after the shock-stall, and then leading to the formation of the BH. In this model, we follow the hydrodynamics until more than 99 % of the materials outside collapse to the BH (typically 2 sec after bounce).

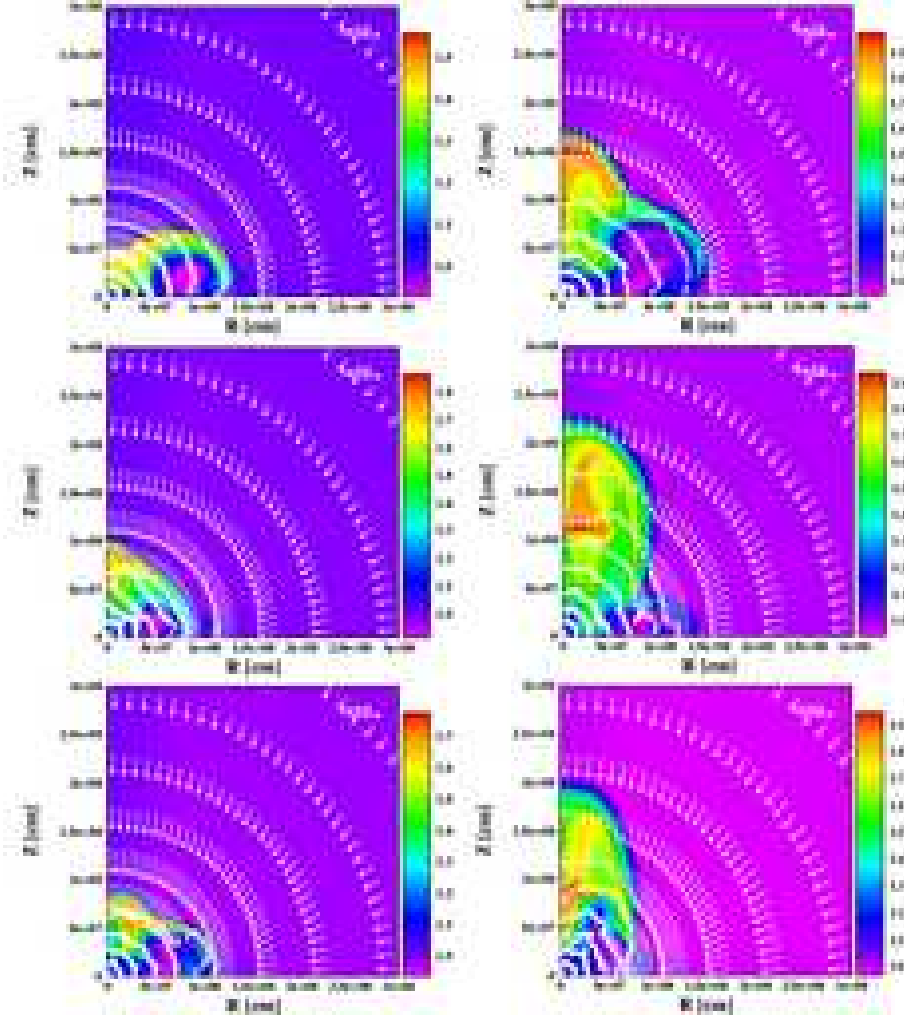


Fig. 5. Entropy profiles of differential rotation model of B10TW1D 50 (left top), 63 (left middle), 73 (left bottom), 87 (right top), 113 (right middle), and 127 (right bottom) ms after bounce, respectively. The color coded contour shows the logarithm of entropy (k_B) per nucleon and arrows represent the velocity fields.

Model B10TW1R thermally bounces rather isotropically in the center, not like model B10TW1D. This is because the central regions have less angular momentum in comparison with the differentially rotating model of B10TW1D. In Figure 6, the time evolutions of entropy after bounce are shown. Unlike B10TW1D (Figure 5), B10TW1R directly collapses to form the BH without producing the outgoing shock waves. This is because the central part has less pressure support from the centrifugal force due to the uniform rotation profile initially imposed. On the other hand, the model B10TW1R has more angular momentum than that of model B10TW1D in the outer part of the core. This leads to the suppression of the accretion rates of the infalling matter to the inner core. As a result, the core of model B10TW1R oscillates in a longer period than that of model B10TW1D because the dynamical timescale, which is proportional to $\rho^{-1/2}$, becomes longer due to the smaller density there.

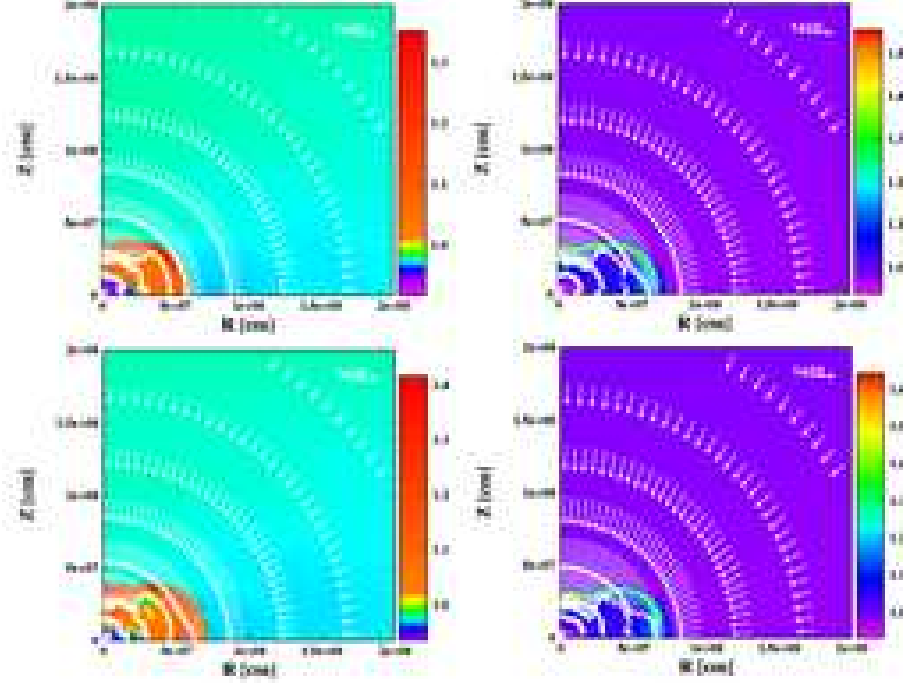


Fig. 6. Same as Figure 5 but for the rigidly rotating model of B10TW1R at 56 (left top), 76 (left bottom), 106 (right top), and 134 (right bottom) ms after bounce, respectively. Color coded contour shows the logarithm of entropy (k_B) per nucleon and arrows represent the velocity fields.

Next we compare the masses of the BH at the formation and the subsequent growth between the two models (see Figure 7). The initial mass of BH of models B10TW1R and B10TW1D are 40 and 70 M_\odot , respectively (see the black filled circles in the Figure). Both of them are larger than that of the spherical collapse model ($\sim 20 M_\odot$). As mentioned, the reason that the earlier formation of less massive BH of model B10TW1R is that the model has smaller centrifugal forces in the central regions than model B10TW1D. On the other hand, reflecting the smaller mass accretion rates to the BH, the growth rate of BH's mass of the model B10TW1R is smaller than that of the model B10TW1D (compare the slopes of the lines in the Figure after the BH formation).

The luminosity of neutrinos and the total leaked energy of the model B10TW1D are shown in the left panel of Figure 8. It is found that the luminosity of μ and τ neutrinos (ν_X) do not overwhelm that of the electron neutrinos even after the bounce unlike the spherical collapse and that most energy are emitted by electron neutrinos (bottom panel). This is because the rotation suppresses the compression of the core, which lowers the temperature in the central regions than that of the spherical model. It should be noted that the energy production rates by the pair annihilation processes sharply depend on the temperature. The neutrino features of B10TW1R are found to be intermediate between the model B10TW1D and the spherical model (see right panels).

If the initial rotation rates of the above two models become larger, the bounce occurs

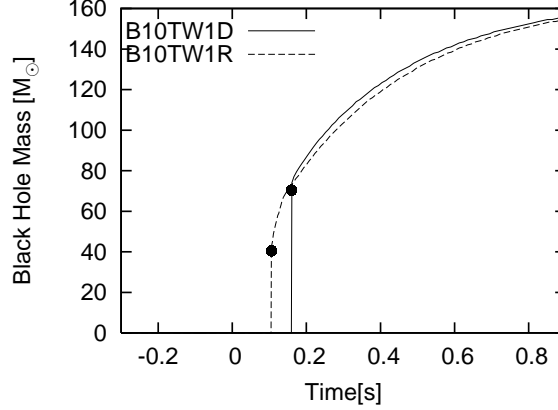


Fig. 7. Evolution of the masses of BH for the rotating models. Solid and dashed lines are for models B10TW1D and B10TW1R, respectively. The black circle indicates the epoch of the black-hole formation. Note that the time is measured from the epoch of the BH formation in the spherical model.

more later due to the stronger centrifugal forces. In addition, the interval of the core oscillations becomes longer. Except for such differences, the hydrodynamic features before the BH formation are mainly determined by the degree of the differential rotation as mentioned above and no qualitative changes are found as the initial rotation rates become larger.

3.2.2. *Effects of Rotation on the BH mass and Neutrino emission*

In this section, we proceed to describe how the initial rotation rate and the degree of the differential rotation affect the growth of the BH masses and the neutrino emissions.

The effects of rotation on the initial masses of the BHs for the almost purely rotating models, labeled by B10, are shown in Figure 9. As seen, larger the initial rotation rate becomes, the heavier BH is found to be produced. This tendency is independent of the degree of the differential rotation. This is simply because rapid rotation tends to halt the infall of the matter to the center, thus heavier masses are required to fulfill the condition of BH formation. It is furthermore found that the initial mass is larger for the differential rotation models than the rigid rotation models. This is regardless of the initial rotation rates. This is due to the smaller angular momentum of the rigid rotation models in the central regions than that of the differential rotation models as mentioned.

In Figure 10, the growth of the BH mass for the corresponding models is shown. It is found that the epoch of the formation is delayed as the initial rotation rates become larger regardless of the degree of the differential rotation. As for the growth rates of BH's mass, it is found that they are almost the same for the differential rotation models regardless of the initial rotation rates (see the left panel of Figure 10). This is because the outer part of the core has little angular momentum due to the strong differential rotation imposed, and thus falls to the center in the similar way. On the other hand, the initial rotation rates affect the evolution of BHs in the rigid rotation models (see the right panel of Figure 10). As the initial rotation

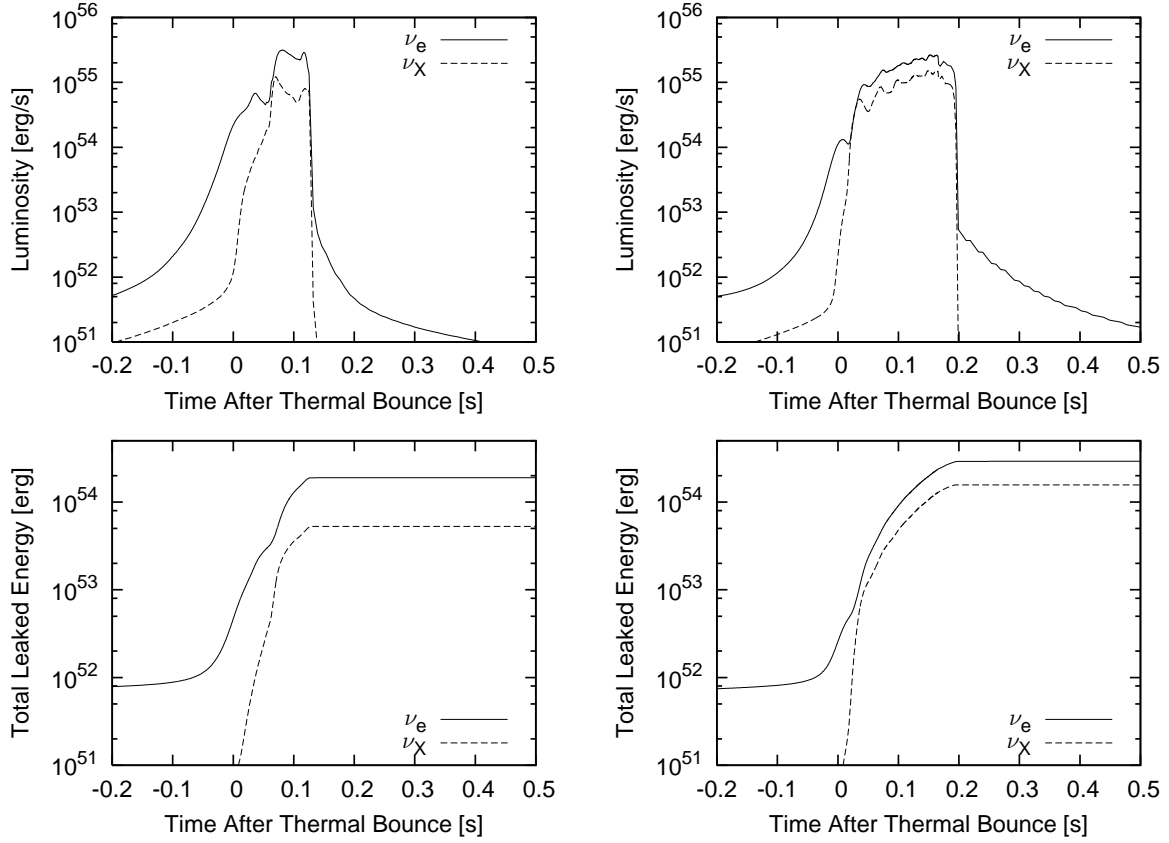


Fig. 8. Same as Figure 3 but for models B10TW1D (left) and B10TW1R (right), respectively.

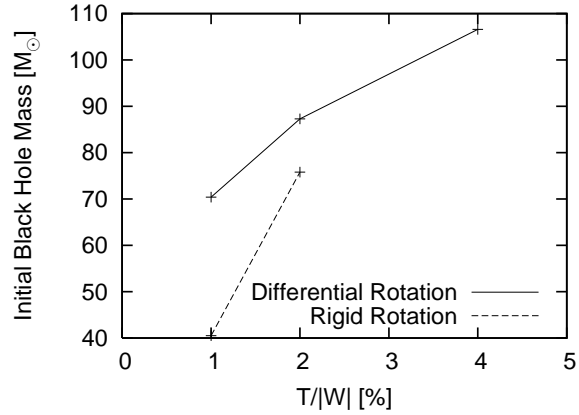


Fig. 9. Effects of initial rotation rate and the degree of differential rotation on the initial mass of the BH. In this figure, the sequence of the models labeled by “B10”, which are almost purely rotating model, is chosen. Note that model B10TW4R is absent because this model does not produce the BH during the simulation time.

rates become larger, the growth rates of the BHs become smaller due to the larger angular momentum imposed initially.

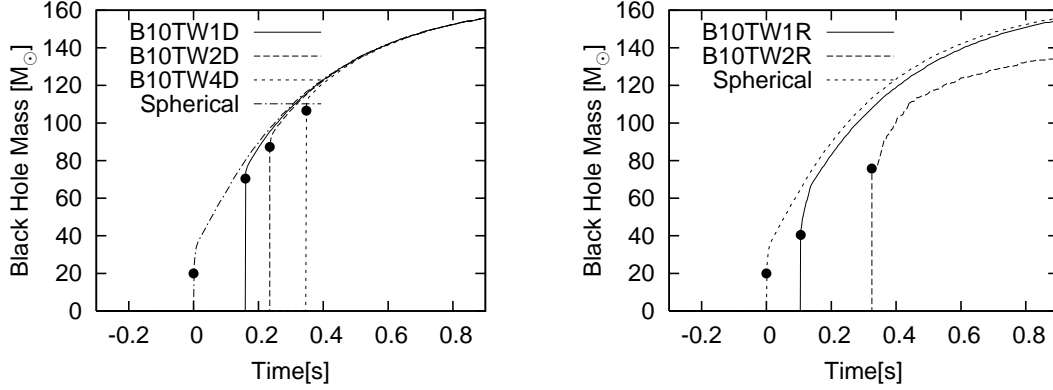


Fig. 10. Time evolution of the BH mass for the almost purely rotating models labeled by B10. *Left panel:* Solid, dashed, dotted, and dashed-dotted lines, are for models B10TW1D, B10TW2D, B10TW4D, and the spherical model, respectively. *Right panel:* Solid, dashed, dotted lines are for models B10TW1R, B10TW2R, and the spherical model, respectively. The time is measured from the thermal bounce of each model. The black filled circles of each panel represent the epoch of the BH formation.

BH's mass at the formation affects the total energy emitted by the neutrinos because the neutrinos in the region of BH cannot escape to the outside of the core afterwards. The total energy emitted by neutrinos are shown in Figure 11. One can see the general trend in the figure that the emitted energy rapidly rises and then becomes constant. The transition to the constant phase corresponds to the formation of the BH.

Also in this case, differential rotation models have similar features after the formation of the BHs (solid line of right panel of Figure 11). It is interesting that the model B10TW2R (dashed line of right panel of Figure 11) by contrast has different behaviors of total emitted energy. This is because this model produces the stable accretion disk around the central BH. As a result, the materials of the disk accretes only slowly to the BH, and thus can emit neutrinos for a longer time. The small accretion rate of this model is also prominent as seen in the Figure 10.

It is interesting to note that only about 10% of the gravitational energy of the core can be carried away by neutrinos even in the most rapidly rotating model considered here (B10TW4D). On the other hand, it is well known that neutrinos carry away 99 % of the gravitational energy of the protoneutron stars in case of the massive stars. The discrepancy stems obviously from the fact that most part of the inner core is absorbed to the BH in case of the Pop III stars.

3.3. Magnetorotational Collapse

In this section, we present the results of the MHD models. First of all, we mention the magnetohydrodynamic (MHD) features in section 3.3.1, then discuss the MHD effects on the

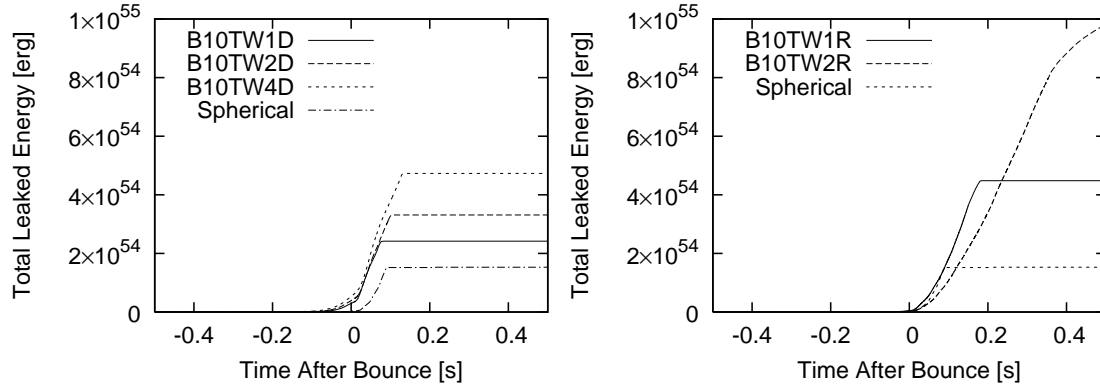


Fig. 11. Time-integrated neutrino leakage energy. *Left panel:* Solid line means B10TW1D, dashed line means B10TW2D, dotted line means B10TW4D and dash-dotted line means Spherical model. *Right panel:* Solid line means B10TW1R, dashed line means B10TW2R and dotted line means Spherical model. The time is measured from the thermal bounce of each model.

BH mass and neutrino emissions in section 3.3.2.

3.3.1. MHD Feature

Amongst the computed models, we find that the models with the strongest magnetic field ($B = 10^{12}\text{G}$) can only produce the jet-like shock waves along the rotational axis, which can propagate outside of the core without shock-stall. First of all, we mention the properties of such models taking model B12TW1D as an example.

The collapse dynamics before bounce is almost the same as the corresponding weak magnetic field model of B10TW1D. This is because the amplified magnetic fields by the compression and the field-wrapping are, of course larger than the weaker field model, but still much smaller than the matter pressure in the central regions. After the bounce, the toroidal magnetic fields produced by the wrapping, provide the additional pressure support, thus acting to push the infalling matter as jetlike outflow rather than rotates along the magnetic field. The jet is launched when the magnetic pressure overcomes the local ram pressure of the accreting matter. This feature is different from another jet driving mechanism, the magneto-centrifugal acceleration (Blandford & Payne 1982).

The MHD features of model B12TW1D after bounce are presented in Figure 12. From the right panels, it is shown that the regions behind the jet-like shock wave ($Z \geq 1.5 \times 10^9 \text{ cm}$) become dilute with the density of $\rho \sim 10^5 \text{ g cm}^{-3}$ and have very high entropy $s \sim 10^2 k_B$. The bottom panel shows the jet is driven by magnetic pressure because the plasma beta (\equiv gas pressure / magnetic pressure) of the region of jet is much smaller than unity. As the jet propagates in the core, a newborn BH is produced (see the white circles of right panels of Figure 12). The mass of the BH is initially $57.9 M_\odot$, which is smaller than the one of B10TW1D ($70.4 M_\odot$). The reason of the difference is mentioned in §3.3.2.

The properties of jet of model B12TW1D are shown in Figure 13. There are profiles of

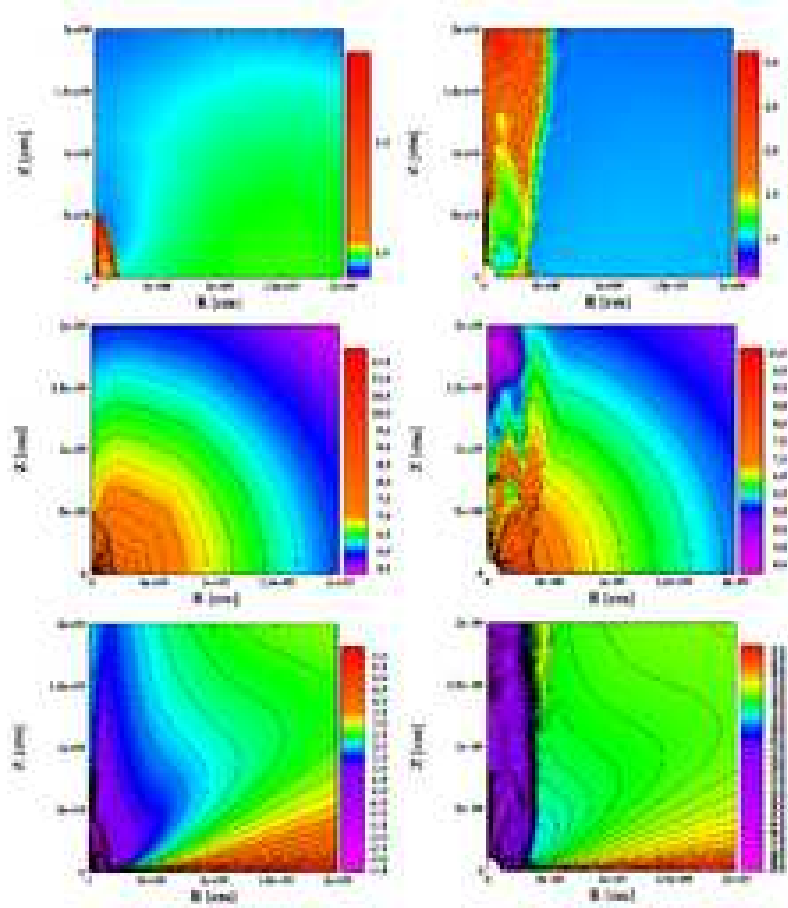


Fig. 12. Time evolution of shock waves of the strongest magnetized model of B12TW1D. The top panel of the figure shows the logarithm of entropy (k_B) per nucleon, the middle panel of the figure shows logarithm of density (g cm^{-3}), and bottom panel shows the logarithm of plasma beta. All left figures are at 119 ms from bounce, and the right figures are at 305 ms. The white circles of the right panels represent the BHs.

density, radial velocity, magnetic field, and pressure at 104 ms after bounce. The density of matter in the jet region is $\sim 10^7 \text{ g cm}^{-3}$. The speed of shock front is as large as 40 % of speed of light, which is mildly relativistic. It is easily seen that the toroidal magnetic field overwhelms the poloidal component behind the shock front. In the inner region, the poloidal magnetic field is larger due to compression. The magnetic pressure overwhelms gas pressure throughout the jet region as already depicted in Figure 12.

Now we move on to discuss how rotation affects the dynamics while fixing the initial field strength. Figure 14 shows the properties of models B12TW1{D,R} and B12TW4{D,R} when the jet-like shock wave reaches to $1 \times 10^9 \text{ cm}$. As clearly seen, the main difference between $T/|W| = 1 \%$ and 4% is the degree of the collimation of the shock wave. As the initial rotation rates become large in the differential rotation models, the compression of the magnetic fields is hindered, thus leading to the suppression of the hoop stress of magnetic fields in the central regions (Takiwaki et al. 2004). As a result, the collimation of the shock wave becomes less

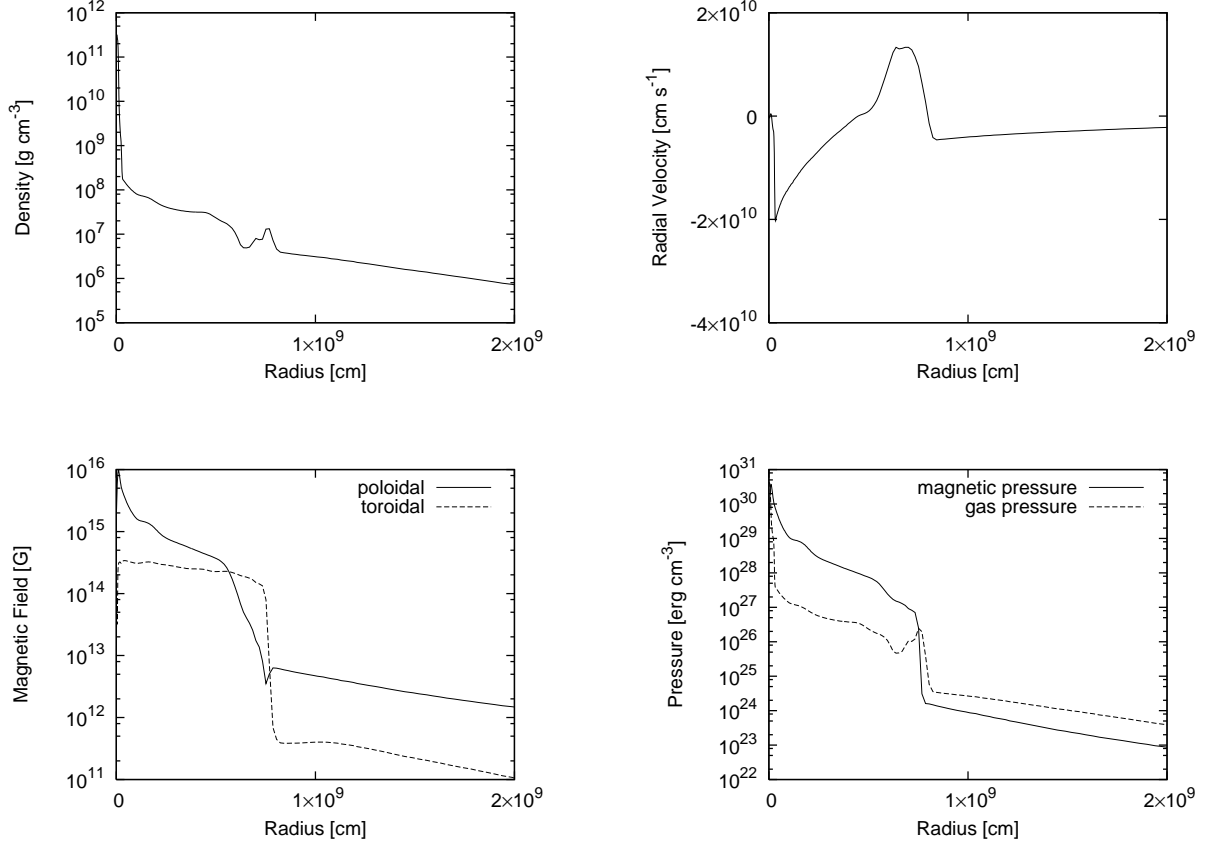


Fig. 13. Various physical quantities around the rotational axis at 104 ms after bounce for model B12TW1D. Density (left top), radial velocity (right top), absolute value of magnetic field (left bottom), and pressure are shown. In the left bottom panel, the solid line and dashed line represent poloidal component and toroidal component, respectively. In the right bottom panel, the dashed line represents gas pressure and solid line represents magnetic pressure.

(compare the top panels). In contrast, the difference of the degree of collimation between models B12TW1R and B12TW4R is smaller than B12TW1D and B12TW4D. This is because the materials in the inner region of rigid rotating models rotate more slowly than the differential models. Thus the degree of the collimation of the shocks depends weakly on the initial $T/|W|$.

Models with the weaker initial magnetic fields do not produce the jet-like explosion except for model B11TW4R. These models collapse to BHs before formation of jets because of weak magnetic pressure. After forming a BH, especially differentially rotating model, rest parts of star rotate slowly so that the magnetic pressure does not grow up. Thus, when BH is formed before jet rises, rest of core only collapse to BH and entire the core are absorbed by BH.

3.3.2. MHD Effects on the BH Mass and Neutrino Emission

The MHD effects on the initial masses of BHs are shown in Tables 2 and 3. As seen, the initial BH mass gets smaller when the initial magnetic field becomes stronger. The angular

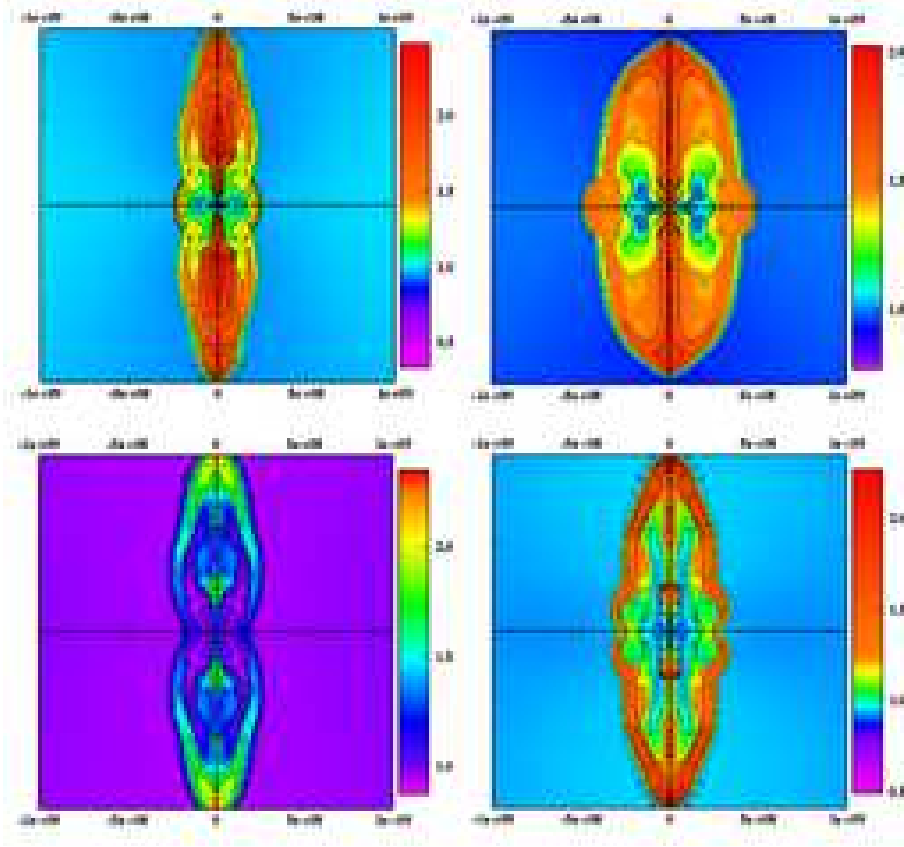


Fig. 14. Profiles of the shock propagation for models B12TW1D (top left), B12TW4D (top right), B12TW1R (bottom left), and B12TW4R (bottom right), respectively. They show the color coded contour plots of logarithm of entropy (k_B) per nucleon. Various profiles are found by changing the strength of the initial magnetic field and rotation.

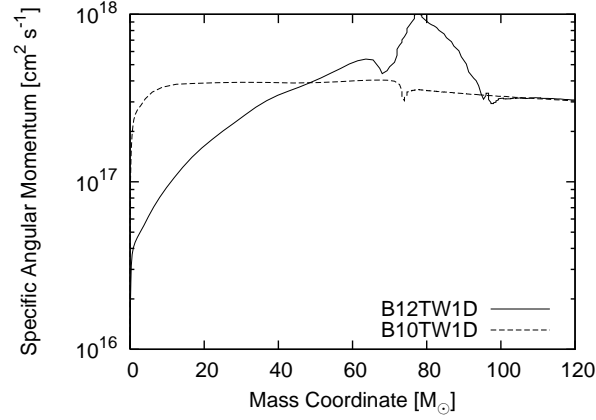
momentum transport by the magnetic fields is an important agent to affect the BH mass. This feature is seen in Figure 15, which represents the distribution of mean specific angular momentum of models B12TW1D and B10TW1D. The central region of B12TW1D has smaller angular momentum than B10TW1D due to angular momentum transport by magnetic fields. The peak of model B12TW1D represents the position of shock front on the equatorial plane. The transport of the angular momentum makes centrifugal force of central region smaller and enhances the collapse. This leads the BH mass smaller. This tendency is more prominent for the rigid rotation models (compare Tables 2 and 3) because the rotation of the central region is slower than differential rotation models and contraction of core is more significant, which leads the amplification of magnetic field and larger angular momentum transport. Figure 16 shows the relation between BH mass and angular momentum at BH formation. The angular momentum of BH gets larger with its mass at the time of BH formation. This is because the matter with large angular momentum cannot collapse due to centrifugal force and requires large

Table 2. Initial Mass of Black Holes for Differentially Rotating Models [M_\odot].

B_0	$T/ W $		
	1%	2%	4%
10^{10}G	70.4	87.3	106.6
10^{11}G	70.4	87.3	106.6
10^{12}G	57.9	75.8	96.6

Table 3. Initial Mass of Black Holes for Rigidly Rotating Models [M_\odot].

B_0	$T/ W $		
	1%	2%	4%
10^{10}G	40.5	75.8	—
10^{11}G	38.6	38.6	—
10^{12}G	15.3	15.1	15.1

**Fig. 15.** Mean specific angular momentum over the shells as a function of the mass coordinate just before BH formation. The solid line and dotted line represent model B12TW1D and B10TW1D, respectively.

amount of accreting matter to collapse BH, as already mentioned in §3.2.

Next, we discuss the MHD effects of neutrino emissions. Figure 17 shows the peak neutrino luminosities as a function of the initial rotation rates. It is shown that the magnetic fields make the peak luminosities smaller, when fixing the initial degree of the differential rotation (compare B10D and B12D, and B10R and B12R). It is noted that the Pop III stars have gentle slope of the density prior to core-collapse, so that materials of the outer region have a great deal of the total gravitational energy of the iron core. Thus the stronger magnetic pressures, which prevent the accretion, make the liberating gravitational energy of the accreting matter smaller, and thus, results in the suppression of the peak luminosities. In case of the rigid rotation, the stronger centrifugal forces in the outer regions, lead to the stronger suppression of the releasable gravitational energy than in the case of the differential rotation. As a result,

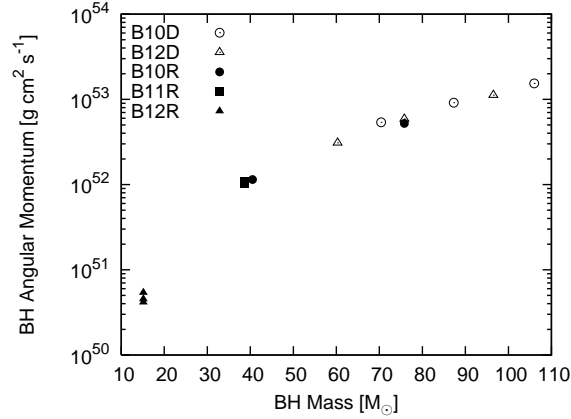


Fig. 16. Relation between BH mass and angular momentum at the BH formation.

the peak luminosities for the rigidly rotating models decreases more steeply with the initial rotation rates than the ones for the differentially rotating models (compare B10R and B10D).

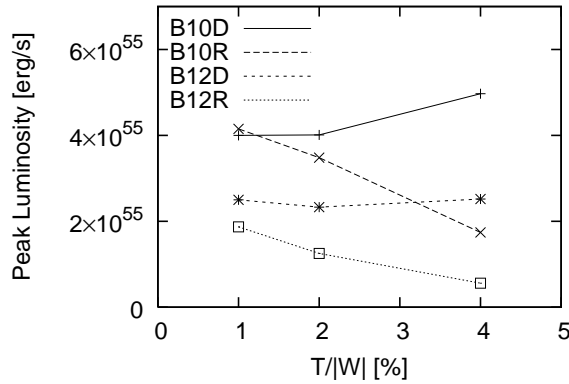


Fig. 17. Effects of rotation and magnetic fields on the peak luminosity of neutrinos.

4. SUMMARY AND DISCUSSION

We studied the magnetorotational core-collapse of Pop III stars by performing the two-dimensional magnetohydrodynamic simulations. Since the distributions of rotation and magnetic fields in the progenitors of Pop III stars are highly uncertain, we changed them in a parametric manner and systematically investigated how rotation and magnetic fields affect the dynamics of Pop III stars. In addition, we explored how rotation and magnetic fields affect the formation of the BHs and the neutrino emissions. In the current Newtonian simulations, the BH formation was ascribed to a certain condition, and after the formation, the central region was excised and treated as an absorbing boundary. As for the microphysics, we took into account the neutrino cooling of 6 species by a leakage scheme with a realistic equation of state. With these computations, we have obtained the following results,

1. In the spherical model, the gravitational contraction is stopped by the gradient of the thermal pressure, not by the nuclear forces as in the case of the massive stars $\approx O(10)M_{\odot}$ with the initial composition of the solar metallicity, because the progenitor of Pop III stars has high entropy, i.e. high temperature initially. Such high temperature also makes different features of the neutrino emissions from the case of the massive stars. The luminosity of μ - and τ - neutrinos dominates over that of the electron neutrinos after core bounce. Thus the gravitational energy of the core is carried away dominantly by μ - and τ - neutrinos.
2. As the initial rotation rates of the core become larger, it is found that the epoch of the BH formation is delayed later and that the initial masses of the BHs become larger. Fixing the initial rotational energy, the BH masses at the formation become larger as the degree of the differential rotation becomes stronger. As the initial degree of the differential rotation becomes larger, the electron neutrino luminosity is found to be more dominant over that of μ and τ neutrinos after core bounce, because the pair creation processes of μ and τ , which sharply depend on the temperature, are more suppressed.
3. We find that the jet-like explosions can be produced even in Pop III stars if the magnetic field is as large as 10^{12}G prior to core-collapse. This jet-like shock wave is completely magneto-driven.
4. Jet-like shocks in the stronger magnetic field models are themselves found to make the initial mass of the BH smaller. The angular momentum transport by magnetic fields is found to be an important agent to make the initial mass of BHs smaller because the transport of the angular momentum enhances the collapse of the central regions. As a result, it is found that the initial BH masses for the most strongly magnetized models are found to become smallest when fixing the initial rotation rates. As for the neutrino luminosities, we point out that the stronger magnetic fields make the peak luminosities smaller, because they can halt the collapse of the materials.

Here we shall refer to the limitations of this study. First of all, we mimicked the neutrino transfer by the leakage scheme. Although the scheme is a radical simplification, we checked that we could reproduce, at least, the qualitative features of the neutrino luminosities. The supremacy of ν_X neutrinos' luminosity in the spherical collapse of Pop III stars obtained in this study is consistent with the foregoing studies by Fryer et al. (2001) and Nakazato et al. (2006), in which the more elaborate neutrino transport schemes were employed. Furthermore, the effects of rotation on the emergent neutrino luminosities are consistent with Fryer & Heger (2000), in which one model of the rotational collapse of the massive stars was investigated. Secondly, the simulations were done with the Newtonian approximation and we defined the BH formation by the marginally stable orbit of a Schwarzschild BH. This treatment is totally inaccurate because the core rotates so rapidly that fully general relativistic (MHD) simulations with the appropriate implementations of the microphysics are necessary, however, are still too computationally prohibitive and beyond our scope of this paper. Remembering these caveats,

this calculation is nothing but a demonstration showing how the combinations of rotation and magnetic fields could produce the variety of the dynamics, and the important consequences in the properties of the neutrino emissions, and these outcomes, of course, should be re-examined by the more sophisticated simulations.

In this study, we followed the dynamics till ~ 1 sec after the formation of the BHs and saw the shock break-out from the cores in the strongly magnetized models. But if we were to follow the dynamics in the much later phase in the weaker magnetized models, the magneto-driven outflows might be produced, due to the long-term field-wrapping and/or the development of the so-called magnetorotational instability, as demonstrated in the study of collapsar (see, e.g., Proga et al. 2003; Fujimoto et al. 2006). But it should be noted that the dynamical phases considered here and the other ones are apparently different (and thus they are complimentary). In the latter studies, the central BHs with a rotationally supported disk around are treated as an initial condition for the computations. Our core-collapse simulations presented here showed that the outer region rotates much slowly than the Keplerian one and most of them directly collapses to BH. Thus the amplification of the magnetic field in the disks, which needs rapid rotation, might not be so efficient as previously demonstrated. To clarify it, we are now preparing for the long-term simulations, in which the final states obtained here are taken as an initial condition.

Then we discuss the validity of the initial strength of the magnetic fields assumed in this study. For the purpose, we estimate the strength of the magnetic field just before collapse with Eq. (13) of Maki & Susa (2004), in which the thermal history of the primordial collapsing clouds was calculated in order to investigate the coupling of the magnetic field with the primordial gas. For example, $B_{\text{ini}} \sim 10^{-7}$ G and $n_{\text{H,ini}} \sim 10^3 \text{ cm}^{-3}$, which are the values they employed, lead $B \sim 10^{11}$ G if the magnetic flux is conserved during the contraction and the clouds collapse to 10^6 g cm^{-3} . Although the above parameters chosen are slightly optimistic, the magnetic fields assumed in this study may not be so unrealistic.

We pointed out that the total neutrino energy emitted from rotation models increases several times than the one of the spherical collapse model. However, the detection of such neutrinos as the diffusive backgrounds might be difficult because the Pop III stars are too distant (see Iocco et al. 2005). Alternatively, the detection of gravitational waves from Pop III stars as the backgrounds seems more likely (Buonanno et al. 2005; Sandick et al. 2006) by the currently planning air-borne laser interferometers such as LISA², DECIGO (Seto et al. 2001) and BBO (Ungarelli et al. 2005), and needs further investigation.

We found that the Pop III stars are able to produce jet-like explosions with mass ejections when the central cores are strongly magnetized. This may be important with respect to its relevance to the nucleosynthesis in such objects (Ohkubo et al. 2006). This is also an interesting topic to be investigated as a sequel of this paper.

² <http://lisa.jpl.nasa.gov>

This study was supported in part by the Japan Society for Promotion of Science (JSPS) Research Fellowships (T.T.), Grants-in-Aid for the Scientific Research from the Ministry of Education, Science and Culture of Japan (No.S14102004, No.14079202, No.17540267, and No.1840044). Numerical computations were in part carried out on VPP5000 at the Center for Computational Astrophysics, CfCA, of the National Astronomical Observatory of Japan.

References

- Abel, T., Bryan, G. L., & Norman, M. L. 2002, *Science*, 295, 93
- Akiyama, S., Wheeler, J. C., Meier, D. L., & Lichtenstadt, I. 2003, *ApJ*, 584, 954
- Ando, S. & Sato, K. 2004, *New Journal of Physics*, 6, 170
- Ardeljan, N. V., Bisnovatyi-Kogan, G. S., & Moiseenko, S. G. 2005, *MNRAS*, 359, 333
- Barkana, R. & Loeb, A. 2001, *Phys. Rep.*, 349, 125
- Blandford, R. D., & Payne, D. G. 1982, *MNRAS*, 199, 883
- Bond, J. R., Arnett, W. D., & Carr, B. J. 1984, *ApJ*, 280, 825
- Bromm, V., Coppi, P. S., & Larson, R. B. 2002, *ApJ*, 564, 23
- Bromm, V. & Larson, R. B. 2004, *ARA&A*, 42, 79
- Bromm, V. & Loeb, A. 2006, *ApJ*, 642, 382
- Buonanno, A., Sigl, G., Raffelt, G. G., Janka, H.-T., & Müller, E. 2005, *Phys. Rev. D*, 72, 084001
- Christlieb, N., et al. 2002, *Nature*, 419, 904
- Daigne, F., Olive, K. A., Vangioni, E., Silk, J., & Audouze, J. 2004, *ApJ*, 617, 693
- Frebel, A., et al. 2005, *Nature*, 434, 871
- Fryer, C. L. & Heger, A. 2000, *ApJ*, 541, 1033
- Fryer, C. L., Woosley, S. E., & Heger, A. 2001, *ApJ*, 550, 372
- Fujimoto, S.-i., Kotake, K., Yamada, S., Hashimoto, M.-a., & Sato, K. 2006, *ApJ*, 644, 1040
- Glover, S. 2005, *Space Sci. Rev.*, 117, 445
- Heger, A., Fryer, C. L., Woosley, S. E., Langer, N., & Hartmann, D. H. 2003, *ApJ*, 591, 288
- Heger, A. & Woosley, S. E. 2002, *ApJ*, 567, 532
- Iocco, F., Mangano, G., Miele, G., Raffelt, G. G., & Serpico, P. D. 2005, *Astroparticle Physics*, 23, 303
- Itoh, N., Adachi, T., Nakagawa, M., Kohyama, Y., & Munakata, H. 1989, *ApJ*, 339, 354
- Iwamoto, N., Umeda, H., Tominaga, N., Nomoto, K., & Maeda, K. 2005, *Science*, 309, 451
- Kotake, K., Sato, K., & Takahashi, K. 2006, *Rep. Prog. Phys.*, 69, 971
- Kotake, K., Sawai, H., Yamada, S., & Sato, K. 2004a, *ApJ*, 608, 391
- Kotake, K., Yamada, S., & Sato, K. 2003, *Phys. Rev. D*, 68, 044023
- Kotake, K., Yamada, S., Sato, K., Sumiyoshi, K., Ono, H., & Suzuki, H. 2004b, *Phys. Rev. D*, 69, 124004
- LeBlanc, J. M. & Wilson, J. R. 1970, *ApJ*, 161, 541
- Maki, H. & Susa, H. 2004, *ApJ*, 609, 467
- Nakamura, F. & Umemura, M. 2001, *ApJ*, 548, 19
- Nakazato, K., Sumiyoshi, K., & Yamada, S. 2006, *ApJ*, 645, 519

- Obergaulinger, M., Aloy, M. A., & Müller, E. 2006, *A&A*, 450, 1107
- Ohkubo, T., Umeda, H., Maeda, K., Nomoto, K., Suzuki, T., Tsuruta, S., & Rees, M. J. 2006, *ApJ*, 645, 1352
- Proga, D., MacFadyen, A. I., Armitage, P. J., & Begelman, M. C. 2003, *ApJL*, 599, L5
- Sandick, P., Olive, K. A., Daigne, F., & Vangioni, E. 2006, *Phys. Rev. D*, 73, 104024
- Sawai, H., Kotake, K., & Yamada, S. 2005, *ApJ*, 631, 446
- Scannapieco, E., Madau, P., Woosley, S., Heger, A., & Ferrara, A. 2005, *ApJ*, 633, 1031
- Schneider, R., Guetta, D., & Ferrara, A. 2002, *MNRAS*, 334, 173
- Seto, N., Kawamura, S., & Nakamura, T. 2001, *Phys. Rev. Lett.*, 87, 221103
- Shen, H., Toki, H., Oyamatsu, K., & Sumiyoshi, K. 1998, *Nucl. Phys. A*, 637, 435
- Stone, J. M. & Norman, M. L. 1992, *ApJS*, 80, 753
- Takiwaki, T., Kotake, K., Nagataki, S., & Sato, K. 2004, *ApJ*, 616, 1086
- Takiwaki, T., Kotake, K., Yamada, S., & Sato, K. 2007, in preparation
- Umeda, H. & Nomoto, K. 2002, *ApJ*, 565, 385
- . 2003, *Nature*, 422, 871
- Ungarelli, C., Corasaniti, P., Mercer, R., & Vecchio, A. 2005, *Class. Quant. Grav.*, 22, S955
- Weinmann, S. M. & Lilly, S. J. 2005, *ApJ*, 624, 526
- Yamada, S. & Sawai, H. 2004, *ApJ*, 608, 907